Thin–Walled Structures 199 (2024) 111800

Contents lists available at ScienceDirect

Thin-Walled Structures

journal homepage: www.elsevier.com/locate/tws

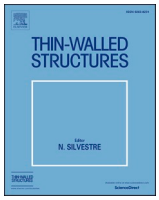

Full length article

Orthotropic mechanical properties of PLA materials fabricated by fused deposition modeling

Meiyu Li [a], Yanan Xu [b], Jianguang Fang [a,*]

[a] School of Civil and Environmental Engineering, University of Technology Sydney, NSW 2007, Australia
[b] School of Aerospace, Mechanical and Mechatronic Engineering, The University of Sydney, Sydney, NSW 2006, Australia

ARTICLE INFO

Keywords:
Fused deposition modeling (FDM)
Mechanical orthotropy
Hill48 yield model
Elastic model
Fracture modes
Ripple defect

ABSTRACT

Polylactic Acid (PLA) sample manufactured by fused deposition modeling (FDM) technique is typically assumed to be transversely isotropic without a thorough examination of its orthotropy in three-dimensional space. This study investigated the mechanical orthotropy of PLA samples with two air gap levels (0 mm and -0.05 mm) and various loading directions. Tensile strength and elastic modulus were experimentally measured and the Hill48 yield model and orthotropic elastic model were calibrated. Results revealed that the anisotropy induced by interlayer bond was more pronounced than that within layer. Introducing a -0.05 mm air gap remarkably reduced voids in printed samples, enhancing the stiffness and strength of tensile samples. It also delayed the transition of fracture modes in intra-layer samples as the filament angle increased from 0° to 90°, which shifted from filament breakage to combined fracture mode and subsequently to interface failure. Despite these improvements, the inherent anisotropy of FDM printed PLA materials remained due to the oriented molecular chains and insufficient chain diffusion. The study emphasizes the importance of orthotropic mechanical models, demonstrating their reliability through calibration with acceptable accuracy.

1. Introduction

Fused deposition modeling (FDM) is one of the most prevalent 3D printing techniques for polymer materials. Owing to advantages of low cost and high design flexibility, FDM printing has been regarded as a replacement for traditional manufacturing process in complex and functional structures [1,2]. A variety of thermoplastic filaments provide various performance of fabricated components [3], such as engineering material Polylactic Acid (PLA), nylon, and high-performance polymer Polyether-ether-ketone (PEEK). Among them, PLA, derived from renewable resources, serves as the predominant feedstock in FDM printing. The biodegradability of PLA holds significant potential in the biomedical field for the production of medical implants and scaffolds [4]. Despite the broad applications, FDM printed parts typically exhibit distinct mechanical performance and high anisotropy compared to their injection-molded counterparts [5]. Printing process parameters such as the layer height [6], raster angle [7], building orientation [8], air gap [9], and printing temperature [10] influence the mechanical behavior of the printed parts, and hence offer opportunities for enhancing the mechanical properties.

With the utilization of FDM printing for fabricating end-use products, the mechanical behavior of FDM parts has gained considerable significance. Various engineering aspects have been explored to facilitate the advancements. For example, fatigue behavior has been investigated [11,12], focusing on the fatigue life of printed parts with different stress levels and structures. Moreover, the impact resistance of printed structures has been studied [13–15]. For example, Chen et al. [13] proposed a novel strategy for printing a nacre-like structure using a single material. The printed structure absorbed impact energy through the fracture of weak bonding interface, achieving higher impact strength of up to six times compared to injection-molded counterpart. The fracture behavior [16–18] and the mechanical strength [19,20] of printed parts have also been explored. These properties were characterized by the inherent anisotropy in the FDM printed parts. For instance, Lampron et al. [17] observed a brittle behavior in inter-layer fracture and a more ductile behavior in cross-layer crack propagation. Samples with unidirectional filaments exhibited up to 60 % anisotropy in tensile strength [21,22].

Insights into the causes of anisotropy in the tensile strength provides guidance for predicting and improving mechanical performance. The prevalent understanding is presented by Gao et al. [23] that the

* Corresponding author.
E-mail address: Jianguang.Fang@uts.edu.au (J. Fang).

https://doi.org/10.1016/j.tws.2024.111800
Received 26 December 2023; Received in revised form 3 March 2024; Accepted 11 March 2024
Available online 12 March 2024

anisotropy of FDM components is dominated by molecular diffusion and entanglement across the bonding interface. The interface strength relies on the amount and distance of molecular chain diffusing across the interface. Based on the reptation model proposed by Dennes and Edwards [24,25], it is implied that the bonding strength in FDM samples mainly depends on the temperature related process parameter such as the printing temperature, cooling rate, and post thermal treatment. Allum et al. [26] argued that the microscale geometry is the predominant cause of strength anisotropy in FDM samples. Inherent to the nature of FDM printing, the deposited filaments are in the shape of flattened ellipses, resulting in partial contact area among filaments and voids in the samples [27]. The calculation on the strength considering actual interlayer contact area affirms that the interlayer bonding strength is comparable to that of the bulk material [28–30]. The numerical simulation conducted by Tronvoll et al. [31] also proved that the anisotropic behavior primarily resulted from the reduction in effective load-bearing cross-sectional area, while the polymer chain diffusion played a secondary role in the anisotropy. From this perspective, mechanical anisotropy of FDM samples can be eliminated by optimizing the geometry-related parameters, such as layer height, line width and air gap.

Based on the above perspectives on the mechanisms of anisotropy, it can be inferred that unidirectional filament samples are mechanically orthotropic in three-dimensional space. However, some researchers classified FDM printed samples as transversely isotropic materials by assuming the filament direction as the principal axis, with planes normal to the filament representing transverse plane [32–34], while others adopted the assumption of transversal isotropy by focusing solely on the anisotropy induced by building direction, neglecting anisotropy within layers caused by raster angle [8,35–37]. A thorough comprehension of the mechanical anisotropy in three-dimensional space is required for accurately predicting the mechanical response of FDM printed samples.

Air gap is an important process parameter to adjust the microstructure and bonding quality [38–40]. Özen et al. [33] observed high porosity and poor bead connections in the non-overlapping configuration but nearly zero microporosity with 20 % overlapping. Ahn et al. [41] found that a negative air gap of -0.08 mm resulted in a noteworthy enhancement of approximately 10 MPa in the tensile strength of samples with 90° raster angle. Although samples with 0° raster angle also experienced strengthening, the effect was comparatively less pronounced. Dawoud et al. [9] noted that by incorporating a -0.05 mm air gap, samples with 90°∘ cross raster angle patterns achieved mechanical properties comparable to those of injection molded parts. A proper air gap has been demonstrated to distinctively enhance mechanical properties and reduce the mechanical anisotropy of FDM printed components. Different from other process parameters such as printing temperature and printing speed, air gap reduces the voids by changing the distance between the filaments without changing the viscosity and thermal conditions of printed parts. Hence, introducing a proper air gap can be a reliable method to explore the mechanisms of anisotropy in FDM samples by minimizing the influence of geometry.

This study aims to characterize the orthotropic properties of FDM printed samples and the effect of air gap through tensile tests and the calibration of orthotropic models. Section 2 introduces the fabrication and experimental protocols, as well as the orthotropic elastic models and yield model for FDM printed material. Section 3 presents experimental results obtained from different anisotropic planes, examining the effects of raster angle, building orientation, and air gap. Section 4 discusses the applicability of orthotropic model and the molecular-scale insight of the orthotropic behavior of FDM material. Section 5 summarizes the research findings and provides an outlook for further research.

2. Experiments and mechanical models

2.1. Fabrication

Premium PLA filament, supplied by Form Futura®, was employed in this study, which possesses a diameter of 2.85 mm. Samples were manufactured on the FDM printer Ultimaker S5. The slicing process was carried out using the open-source software, Cura [42], to convert the 3D model into a layer-by-layer and line-by-line format. During this process, specific process parameters were assigned as shown in Table 1. The tensile samples were sliced using a 'Line' infill pattern, where the lines were orientated along a fixed direction, resulting in a unidirectional infill structure. To examine the influence of air gap, the distance between raster was set to 0.8 mm and 0.75 mm, respectively, while maintaining a constant line width of 0.8 mm as shown in Fig. 1(a). Consequently, samples with air gaps of zero and -0.05 mm were obtained.

The microstructure of FDM samples is significantly influenced by the layer thickness and line width. Özen et al. [33] observed that a lower ratio of the layer thickness to line width contributed a more compact microstructure in FDM samples. Hence, the line width of 0.8 mm companied by a 0.2 mm layer thickness was determined. In this context, the introduction of a negative air gap has the potential to eliminate micro-voids in the printed samples. Printing temperature governs the viscosity and flow characteristics of melted polymer, affecting the morphology of the deposited filaments and the strength of printed samples [43,44]. A printing temperature of 210 °C was chosen to represent the typical printing conditions for PLA filaments. A bed temperature of 60 °C was chosen to prevent the warpage and detachment of samples from platform caused by high thermal gradient. Samples printed at 60 °C bed temperature exhibited a slightly higher strength (about 1.5 MPa) than those printed at 30 °C in the preliminary tests, while elastic modulus was barely affected by bed temperature. Both excessively high and low printing speeds can lead to defects in extruded filaments. For example, Geng et al. [45] observed a large amount of cavity on the surface of PEEK filament at a low printing speed of 6.9 mm/min. Bakrani Balani et al. [46] reported the 'sharkskin' defect in PLA extruded at high velocity, characterized by a wavy shape of the filaments. To ensure the stability of printing, the printing speed of 45 mm/s was employed in this study.

2.2. Experimental set-up

In this study, dog-bone samples were designed in accordance with the Type I specifications of the ASTM D638 standard. Type I sample possesses an overall length of 165 mm with a gage length of 50 mm. The selected thickness is 4 mm. To investigate the orthotropic nature of FDM printed materials, two right-hand coordinates systems were established for tensile samples and material separately. The global coordinate system $\{O, x, y, z\}$ was utilized for dog-bone samples with x-axis representing the tensile loading directions, while the y and z axes denoted the width and thickness, respectively. In addition, a material coordinate

Table 1
FDM printing parameters.

Process parameter	Configuration
Layer height	0.2 mm
Line width	0.8 mm
Infill pattern	Line
Distance between lines	0.8 mm, 0.75 mm
Line direction	90°
Printing temperature	210 °C
Printing speed	45 mm/s
Fan speed	100 %
Bed temperature	60 °C

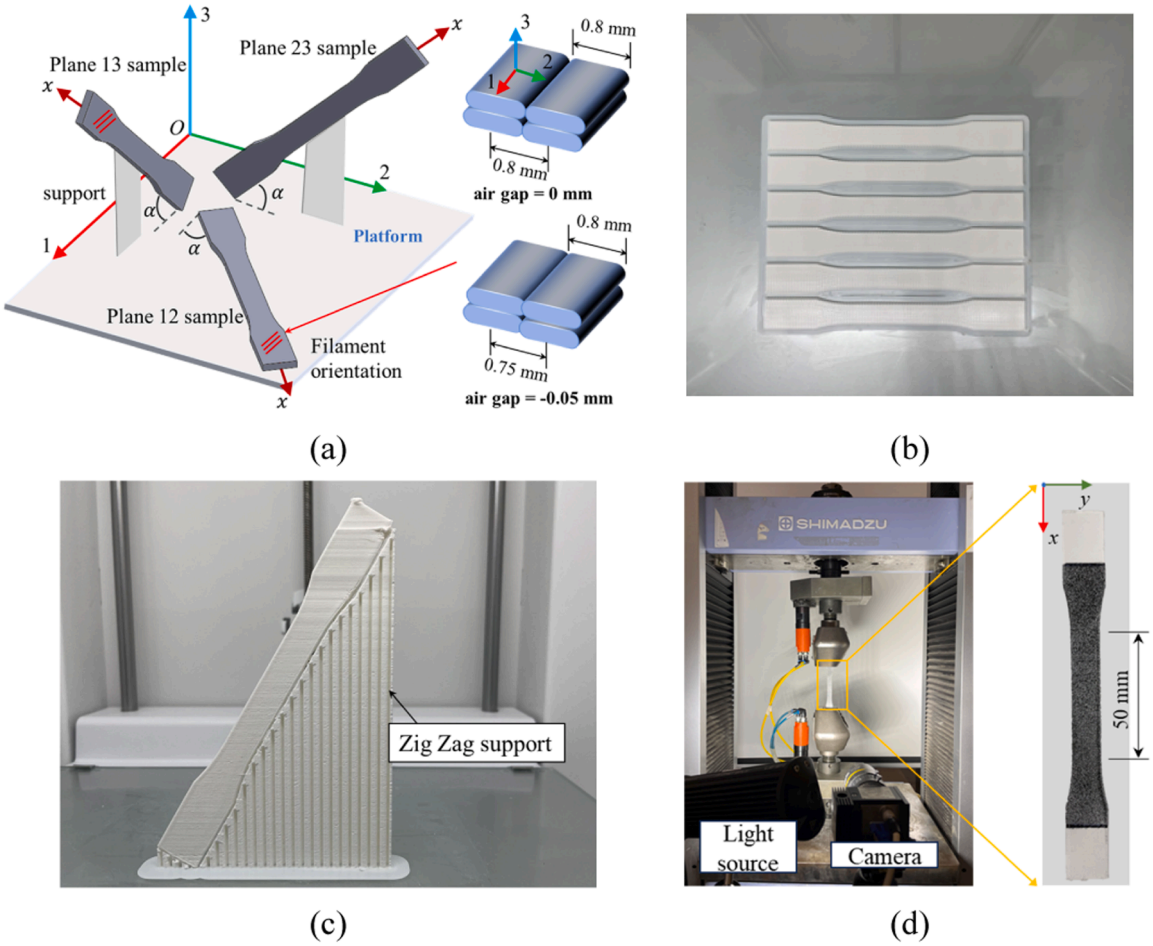

Fig. 1. Sample design and experimental setup (a) dog-bone samples rotating in different planes with varying air gaps, (b) Plane 12 samples, (c) Plane 13 sample upheld by a zig-zag support, and (d) tensile tests with DIC system (gauge length 50 mm).

system denoted as {*O*, 1, 2, 3} was employed as depicted in Fig. 1(a). In this system, filaments were extruded along the axis 1 and deposited along the axis 2 in a line-by-line manner. The subsequent layers were then stacked along axis 3 to form the finial printed parts.

Three groups of tensile samples were designed to explore the orthotropic behavior of FDM printed samples, as depicted in Fig. 1(a). These samples underwent rotation in three distinct material planes: Plane 12, Plane 13, and Plane 23. In each plane, the rotation angle of samples, denoted as α, varied from 0° to 90° at 15° intervals. To achieve a reliable result, 6 replicate samples were printed at each angle. The samples in Plane 12 and Plane 13 are shown in Fig. 1(b) and (c). Zig Zag supports were printed to uphold the Plane 13 samples and Plane 23 samples.

The uniaxial tensile tests were conducted in accordance with the ASTM D638-14 standard. As shown in Fig. 1(b), a universal material testing machine (AGX-50 kN, Shimadzu, Japan) equipped with a 5 kN load cell was employed to conduct the experiments, maintaining a constant displacement loading rate of 5 mm/min. Digital image correlation (DIC) technique was used to measure strain where the samples were colored to create speckle patterns. Besides, microscopy analyzes were performed with scanning electron microscope (SEM) to characterize the microstructure of the PLA samples with different air gaps and rotation angles.

2.3. Orthotropic elastic model and yield model

2.3.1. Hill48 yield model

The Hill48 model was adopted to describe the orthotropic ultimate strength in three-dimension [32,47]. The quadratic Hill48 yield model has the form:

$$F(\sigma_{22}-\sigma_{33})^2+G(\sigma_{33}-\sigma_{11})^2+H(\sigma_{11}-\sigma_{22})^2+2L\sigma_{23}^2+2M\sigma_{31}^2+2N\sigma_{12}^2=1 \quad (1)$$

where F, G, H, L, M, N are the orthotropic parameters that need to be determined experimentally.

The stress matrix is denoted as σ in the material coordinate system {O, 1, 2, 3}, whereas it is referred to as σ' in the global coordinate system {O, *x, y, z*}. To calibrate the Hill48 yield model, the stress obtained from global coordinate system is transformed to material coordinate system as follows:

$$\sigma=\mathbf{R}\sigma'\mathbf{R}^{\mathrm{T}} \quad (2)$$

where **R** is the rotation matrix defined by:

$$\mathbf{R} = \begin{bmatrix} l_1 & m_1 & n_1 \\ l_2 & m_2 & n_2 \\ l_3 & m_3 & n_3 \end{bmatrix} \tag{3}$$

Here, $l_i,\ m_i, n_i\ (i = 1,\ 2,\ 3)$ are the direction cosine of angles between axes of two coordinate systems. For example, l_1 is the cosine of the angle between 1 and x.

Utilizing the Voigt notation, the stress transformation in Eq. (2) can be expressed as

$$\begin{bmatrix} \sigma_1 \\ \sigma_2 \\ \sigma_3 \\ \tau_{12} \\ \tau_{23} \\ \tau_{31} \end{bmatrix} = \mathbf{R}_\sigma \begin{bmatrix} \sigma_x \\ \sigma_y \\ \sigma_z \\ \tau_{xy} \\ \tau_{yz} \\ \tau_{zx} \end{bmatrix} \tag{4}$$

Here, the stress transformation matrix, $\mathbf{R}_\sigma$, is

$$\mathbf{R}_\sigma = \begin{bmatrix} l_1^2 & m_1^2 & n_1^2 & 2l_1m_1 & 2m_1n_1 & 2l_1n_1 \\ l_2^2 & m_2^2 & n_2^2 & 2l_2m_2 & 2m_2n_2 & 2l_2n_2 \\ l_3^2 & m_3^2 & n_3^2 & 2l_3m_3 & 2m_3n_3 & 2l_3n_3 \\ l_1l_2 & m_1m_2 & n_1n_2 & l_1m_2 + l_2m_1 & m_1n_2 + m_2n_1 & l_1n_2 + l_2n_1 \\ l_2l_3 & m_2m_3 & n_2n_3 & l_2m_3 + l_3m_2 & m_2n_3 + m_3n_2 & l_2n_3 + l_3n_2 \\ l_1l_3 & m_1m_3 & n_1n_3 & l_1m_3 + l_3m_1 & m_1n_3 + m_3n_1 & l_1n_3 + l_3n_1 \end{bmatrix} \tag{5}$$

When the samples reach failure, the stress matrix is transformed to material coordinate system. With these transformed stress matrices, the Hill48 yield model can be calibrated using the regression analysis method. This method facilitates the determination of optimal fitting values for the orthotropy parameters that align with the experimental data.

2.3.2. Elastic compliance matrix

In three-dimensional modeling, the generalized Hook's law can be written in the vectorial form as follows:

$$\varepsilon = \mathbf{S}\sigma \tag{6}$$

where ε is the strain, $\mathbf{S}$ is the elastic compliance. This equation could be expressed in a matrix form for orthotropic materials as:

$$\begin{bmatrix} \varepsilon_1 \\ \varepsilon_2 \\ \varepsilon_3 \\ \gamma_{12} \\ \gamma_{23} \\ \gamma_{31} \end{bmatrix} = \begin{bmatrix} \frac{1}{E_1} & -\frac{v_{21}}{E_2} & -\frac{v_{31}}{E_3} & 0 & 0 & 0 \\ -\frac{v_{12}}{E_1} & \frac{1}{E_2} & -\frac{v_{32}}{E_3} & 0 & 0 & 0 \\ -\frac{v_{13}}{E_1} & -\frac{v_{23}}{E_2} & \frac{1}{E_3} & 0 & 0 & 0 \\ 0 & 0 & 0 & \frac{1}{G_{12}} & 0 & 0 \\ 0 & 0 & 0 & 0 & \frac{1}{G_{23}} & 0 \\ 0 & 0 & 0 & 0 & 0 & \frac{1}{G_{31}} \end{bmatrix} \begin{bmatrix} \sigma_1 \\ \sigma_2 \\ \sigma_3 \\ \tau_{12} \\ \tau_{23} \\ \tau_{31} \end{bmatrix} \tag{7}$$

where E_1, E_2, E_3 represent the Young's moduli along 1, 2 and 3 axes in material coordinate system as shown in Fig. 2(b), respectively. G_{12}, G_{23}, and G_{31} are the shear moduli in Plane 12, 23, and 31. v_{ij} $(i,\ j\ = 1,\ 2,\ 3)$ is the Poisson's ratio where the subscripts represent that the strain in j direction is caused by the loading along i direction. There are 9 independent factors in elastic compliance of orthotropic material due to the symmetry requirements as shown below.

$$\frac{v_{ij}}{E_i} = \frac{v_{ji}}{E_j} \tag{8}$$

The strain was transformed from matrix coordinate system to global coordinate system by

$$\varepsilon' = \mathbf{R}^{\mathrm{T}}\varepsilon\mathbf{R} \tag{9}$$

It is denoted as the following equation using the Voigt notation.

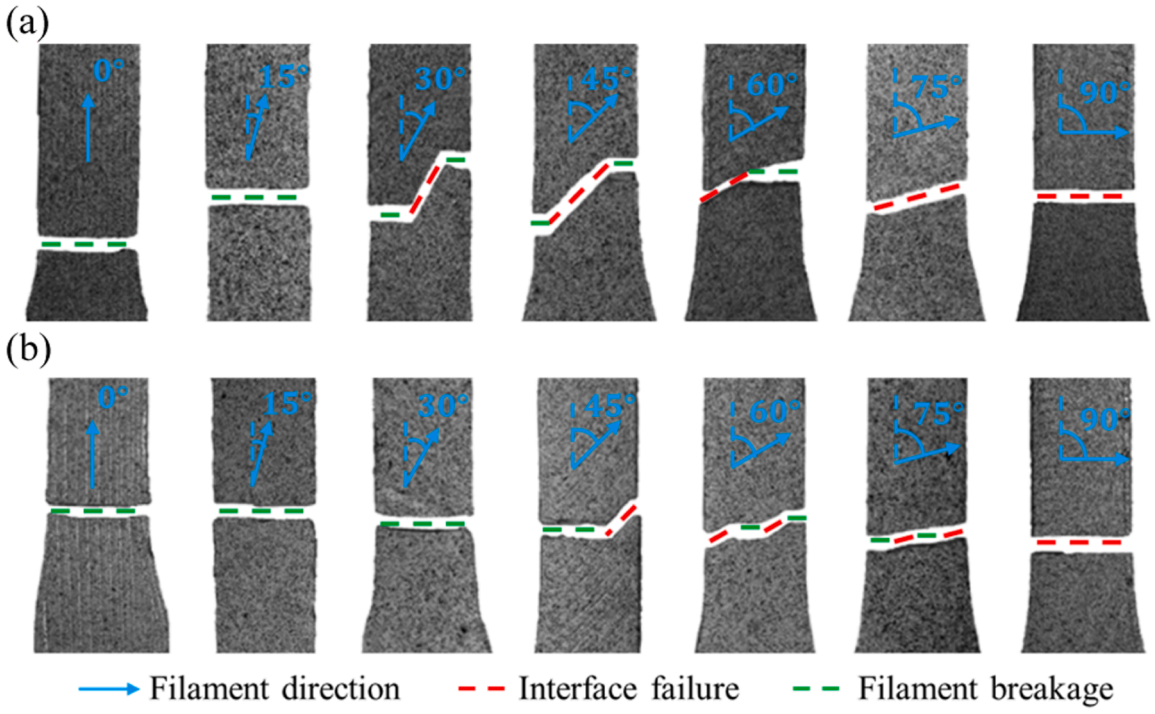

Fig. 2. Fractured samples in Plane 12 with (a) air gap = 0 mm, and (b) air gap = −0.05 mm.

$$\begin{bmatrix} \varepsilon_x \\ \varepsilon_y \\ \varepsilon_z \\ \gamma_{xy} \\ \gamma_{yz} \\ \gamma_{xz} \end{bmatrix} = R_\varepsilon^{'} \begin{bmatrix} \varepsilon_1 \\ \varepsilon_2 \\ \varepsilon_3 \\ \gamma_{12} \\ \gamma_{23} \\ \gamma_{13} \end{bmatrix} \tag{10}$$

where the transformation matrix for strain is expressed as:

$$\boldsymbol{R}_{\boldsymbol{\varepsilon}}^{'} = \begin{bmatrix} l_1^2 & l_2^2 & l_3^2 & l_1 l_2 & l_2 l_3 & l_1 l_3 \\ m_1^2 & m_2^2 & m_3^2 & m_1 m_2 & m_2 m_3 & m_1 m_3 \\ n_1^2 & n_2^2 & n_3^2 & n_1 n_2 & n_2 n_3 & n_1 n_3 \\ 2l_1 m_1 & 2l_2 m_2 & 2l_3 m_3 & l_1 m_2 + l_2 m_1 & l_2 m_3 + l_3 m_2 & l_1 m_3 + l_3 m_1 \\ 2m_1 n_1 & 2m_2 n_2 & 2m_3 n_3 & m_1 n_2 + m_2 n_1 & m_2 n_3 + m_3 n_2 & m_1 n_3 + m_3 n_1 \\ 2l_1 n_1 & 2l_2 n_2 & 2l_3 n_3 & l_1 n_2 + l_2 n_1 & l_2 n_3 + l_3 n_2 & l_1 n_3 + l_3 n_1 \end{bmatrix} \tag{11}$$

Substituting Eqs. (4) and (6) into (10), we obtain

$$S^{'} = R_\varepsilon^{'} S R_\sigma \tag{12}$$

It is clear from Eqs. (5) and (11) that the transformation matrix for strain from the material to the global coordinate system is equal to the transposed matrix of the stress transformation matrix, i.e.,

$$R_\varepsilon^{'} = R_\sigma^T \tag{13}$$

Eq. (12) can be written as

$$\mathbf{S}^{'} = \mathbf{R}_\sigma^{\mathrm{T}} \mathbf{S} \mathbf{R}_\sigma \tag{14}$$

Corresponding to Eq. (10), $1/E_x$ represents the first element of elastic compliance $S^{'}$ in global coordinate system. In the uniaxial tensile tests, E_x can be directly derived from the stress-strain curves.

3. Results

The included angle between filaments and the specimen axis (loading direction), denoted as the filament angle, changes with the rotation of samples in both Plane 12 and Plane 13. The difference is that the Plane 12 samples emphasize the intra-layer mechanical anisotropy caused by raster angle while Plane 13 samples highlight the anisotropy induced by building orientation. In the section, experimental results are presented focusing on each plane to illustrate orthotropic behavior of FDM materials and the impact of air gap.

3.1. Intra-layer mechanical properties in Plane 12

3.1.1. Impact of air gaps on the transition of fracture modes

The fractured samples after tensile experiments were shown in Fig. 2, revealing three types of fracture modes: filament breakage, interface failure, and combined fracture. With a 0 mm air gap (Fig. 2(a)), samples at 0° and 15° exhibited filament breakage where the fracture surface were perpendicular to the tensile direction, while those at 30° to 60° displayed a combined fracture mode characterized by both filament breakage and interface failure. The interface failure developed parallel to the filament direction. As the rotation angle increased to 75° and 90°, fractures were caused solely by interface failure.

Interestingly, when the air gap decreased to -0.05 mm, a transition in fracture modes was observed in samples at 30° and 75°, as shown in Fig. 2(b). The fracture mode in samples at 30° shifted from a combined fracture mode to filament breakage, while in samples at 75°, it transitioned from interface failure to combined fracture mode. Although the fracture modes of other samples remained consistent, sample at 45° was primarily characterized by filament breakage in the combined fracture mode, rather than interface failure in the case of 0 mm air gap. Hence, the negative air gap delayed the transition of fracture mode as raster angle increased, from filament breakage to interface failure of Plane 12 samples.

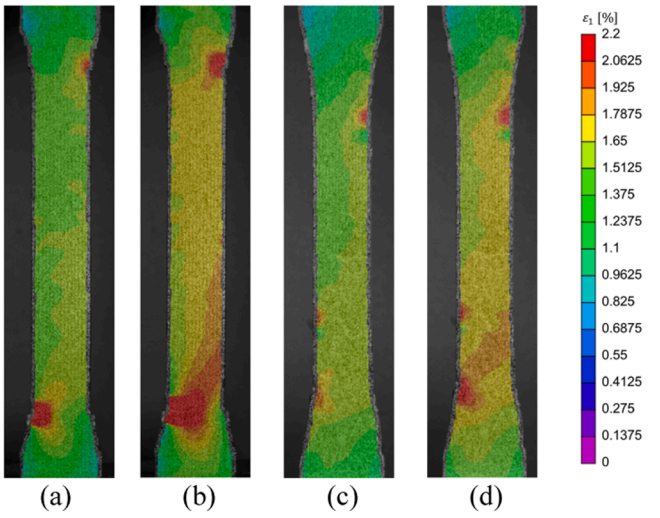

Fig. 3. Contour of maximum principal strain ε_1 for 0° samples at (a and b) 0 mm, and (c and d) -0.05 mm air gap, with ε_y at 1.5 % and 1.7 %.

However, some fractures occurred outside the measurement area of the tensile sample, for example, the sample at 0°. Fig. 3 presented the contours depicting the maximum principal strain at different strain ratios to illustrate the deformation of samples at 0° prior to fracture. It was observed that the strain was uniformly distributed within the measurement section of the sample, with notable strain concentration at the end of fillet radius area. The concentration became more pronounced with the increase of strain. Given the line width of 0.8 mm, the filament termination at these areas caused significant variation of 1.6 mm in cross section, leading to stress concentration and consequently, premature fracture [48]. However, reducing the air gap to -0.05 mm contributed to a rather continuous dimensional variation in the radius area, reducing the strain localization.

The delay of fracture mode transition resulted from the improved interface bonding quality achieved by the denser microstructure. Reducing the distance between filaments with a -0.05 mm air gap necessitates the extrusion of more filaments to achieve the designed dimensions. Table 2 compares the masses of samples with varying air gaps, considering the estimated mass derived from the G-code and the actual mass. There was an expected extrusion of 5.30 % more material by G-code mass when the air gap decreases to -0.05 mm, while the increase of actual mass ranged from 3.27 % to 5.53 %. The actual mass of the printed samples was consistently lower than the G-code mass, which may be attributed to material underflow resulting from slippage between rollers and filaments [49].

SEM images in Fig. 4 show the fracture surfaces of samples at 0° and 90° with different air gaps. The fracture surface of the sample at

Table 2
Estimated and actual mass of samples with different air gaps.

Rotation angle (°)	Zero air gap		Negative air gap		Expected increase (%)	Actual increase (%)
	G-code mass (g)	Actual mass (g)	G-code mass (g)	Actual mass (g)		
0	13.01	12.59	13.70	13.17	5.30	4.61
15		12.81		13.34		4.14
30		12.85		13.27		3.27
45		12.62		13.32		5.47
60		12.78		13.21		3.36
75		12.82		13.48		5.53
90		12.90		13.32		4.10

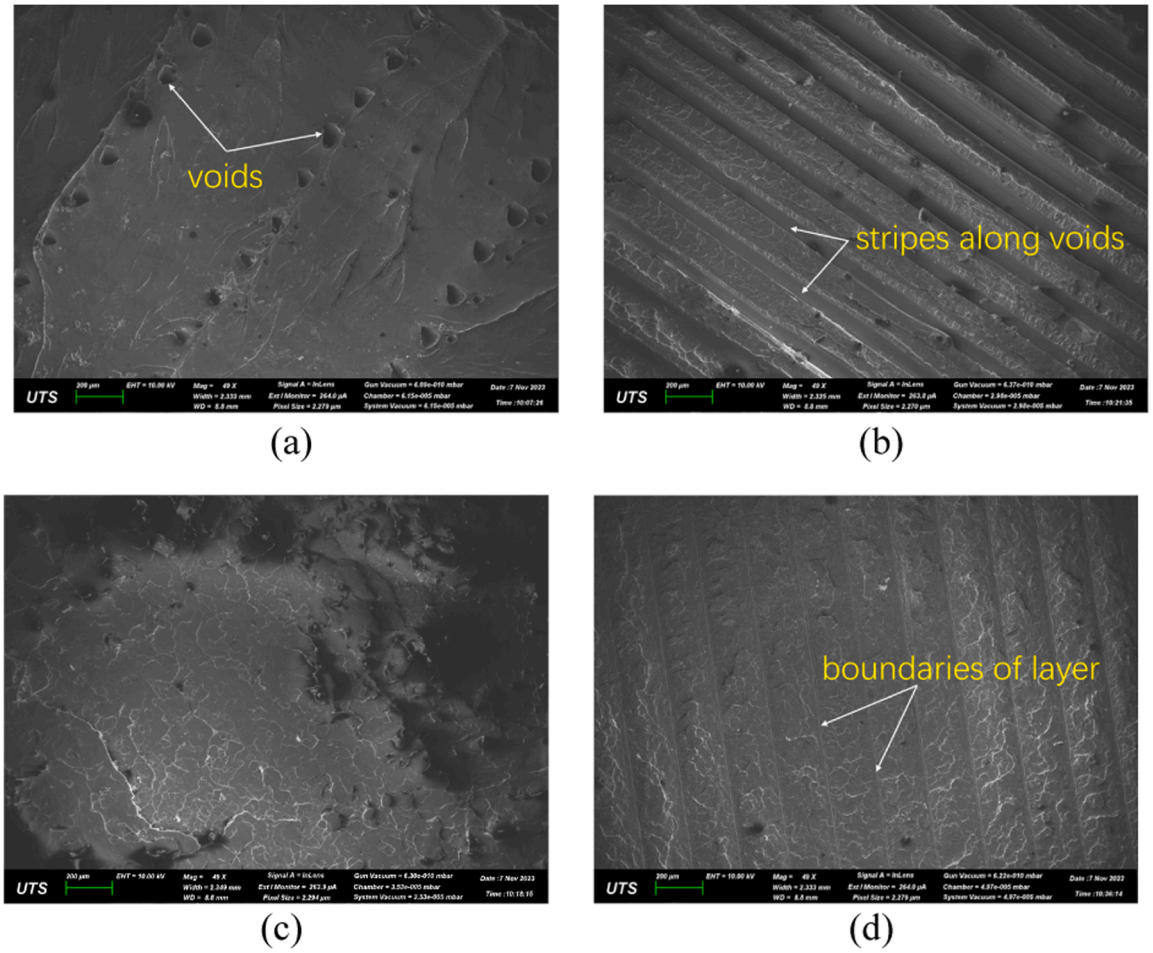

Fig. 4. SEM images of fracture surfaces of Plane 12 samples with air gap = 0 mm at (a) 0° and (b) 90° and air gap = -0.05 mm at (c) 0° and (d) 90°

0° reveals filament breakage occurring perpendicular to the filaments. When the air gap was 0 mm (Fig. 4(a)), numerous voids were observed between the filaments, leading to the clear visibility of the bead boundaries. The voids appeared as stripes in sample at 90° in Fig. 4(b), negatively impacting the bonding area between filaments. By contrast, the fracture surface of sample at 0° with the -0.05 mm air gap (Fig. 4(c)) exhibited a completely dense and homogenous characteristic, with an absence of line and layer features as well as voids. In sample at 90° (Fig. 4(d)), the stripes along voids almost disappeared and showed the boundaries of printing layer. The bonding area was enlarged to the same as the layer thickness, ensuring a reliable contact between the filaments.

3.1.2. *Tensile results with different air gaps*

The stress-strain curves of samples with varying rotation angles and

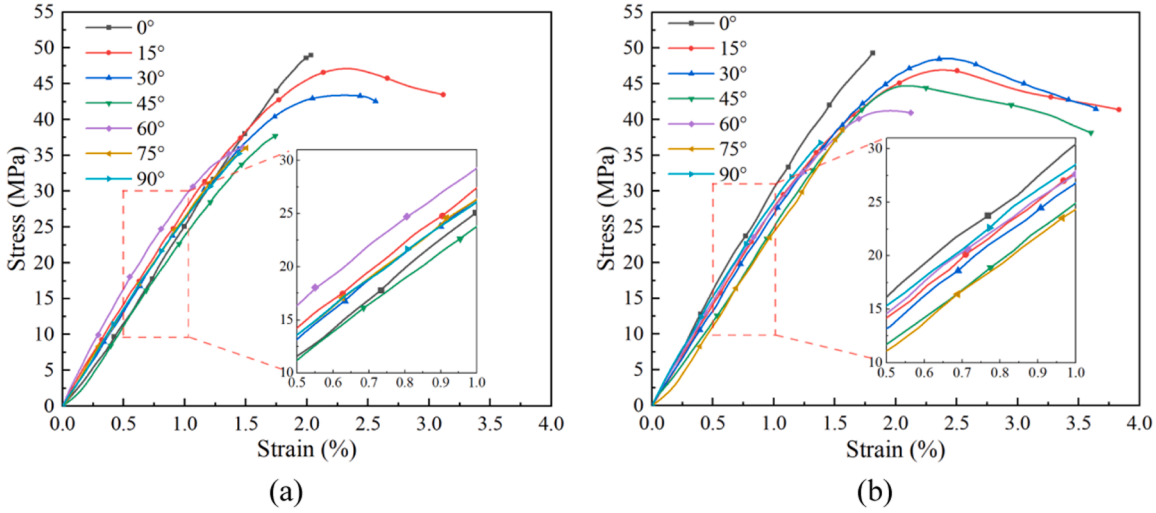

Fig. 5. Stress-strain curves of tensile samples in Plane 12, (a) air gap = 0 mm, and (b) air gap = -0.05 mm.

air gaps were presented in Fig. 5. The curves of samples with small rotation angles exhibited plastic deformation stage after reaching their ultimate tensile strength (UTS) except sample at 0°. The brittle fracture of the sample at 0° was attributed to a premature fracture induced by strain concentration as illustrated in Fig. 3. When the air gap was 0 mm, samples at 15° and 30° exhibited a plastic stage in their stress-strain curves after reaching their UTS. In comparison, the plastic stage in the stress-strain curves was observed in samples ranging from 15° to 60° when the air gap decreased to -0.05 mm. Corresponding to their fracture modes, these samples that experienced filament breakage or combined fracture mode possessed a plastic deformation stage. Conversely, samples with interface failure show brittle fractures. Moreover, samples with -0.05 mm air gap possessed a larger elongation at breakage compared to those with 0 mm air gap.

Given that all samples reached their UTS within a strain ratio ranging from 1.5 % to 2.5 %, the slope of the stress-strain curves between strain ratios of 0.5 % to 1.0 % (enlarged section in Fig. 5) was utilized to calculate the tensile elastic modulus for the samples. The elastic modulus and UTS were presented in Figs. 6(a) and (b), respectively. The filament angle had a slight impact on the elastic modulus of samples in Plane 12. When the air gap was 0 mm, the maximum value was 2697 MPa, obtained from samples at 0°. Then, the elastic modulus slightly decreased with an increase of rotation angle, reaching the minimum value of 2575 MPa at 90°. Due to the presence of -0.05 mm air gap, elastic modulus showed an improvement ranging from 1.2 % to 3.6 % and an average increasement of 2.1 % in Plane 12. Specifically, the elastic modulus increased to 2760 MPa at 0° and 2649 MPa at 90°.

The filament angle exhibited more pronounced influence on the UTS as shown in Fig. 6(b). When the air gap was 0 mm, the experimental results significantly decreased with the rotation angle except for sample at 0°. Due to the premature fracture illustrated in Section 3.1.1, samples at 0° possess a smaller UTS compared to samples at 15°. When the rotation angle increased from 15° to 45°, the UTS experienced a significant drop, decreasing from 46.6 MPa to 39.1 MPa. Simultaneously, the fracture mode shifted from filament breakage at 15° to combined fracture at 45°. As the rotation angle further increased from 45° to 90°, the decrease was only 3.9 MPa. The enhancement induced by the negative air gap varies with different rotation angles. When the rotation angle exceeded 15°, the UTS of samples exhibited significant improvement. The transition in fracture mode observed in samples at 30° and 75° also highlighted the improvement of filament-to-filament bonding strength. The maximum percentage increase in UTS occurred in the sample at 30°, reaching 14.9 %, while those for samples at 0° and 15° were slightly lower. Overall, the -0.05 mm air gap increased the UTS by an average of 8.9 % in Plane 12.

Furthermore, replicated samples with 0 mm air gap demonstrated higher standard deviations in both elastic modulus and strength. When the air gap is 0 mm, the standard deviation of modulus ranged from 60 to 110 MPa and obtained its maximum at 75° rotation angle. However, it was less than 40 MPa in the case of -0.05 mm air gap. A similar trend was observed in UTS where samples with a -0.05 mm air gap exhibited reduced dispersion in each group. The low dispersion in the -0.05 mm groups was attributed to reliable bonding quality between filaments. As the shape of the extruded filament is elliptical, samples with a 0 mm air gap were susceptible to printing uncertainties, including variations in filament diameter, deposition shape, machine axes alignments, and position precision [50]. These uncertainties impact fabrication accuracy and repeatability of the replicate samples. Hence, the negative air gap helps to minimize the effects of fabrication uncertainties.

3.2. Effect of interlayer bonding on mechanical behavior in Plane 13

3.2.1. Fracture modes of samples in Plane 13

Similar to the samples in Plane 12, three fracture modes were observed. Fig. 7(a) shows the fractured samples with 0 mm air gap. Samples at 0° and 15° exhibited filament breakage, while samples at 30° and 45° showed combined fracture mode. The interface failure mode occurred when rotation angle was higher than 60° which was earlier than samples in Plane 12. It indicated that the interlayer bonding strength was lower than the filament bonding strength within layers. Another distinction from the sample in Plane 12 is that the fracture mode at all rotation angles remained unchanged when the air gap decreased to -0.05 mm.

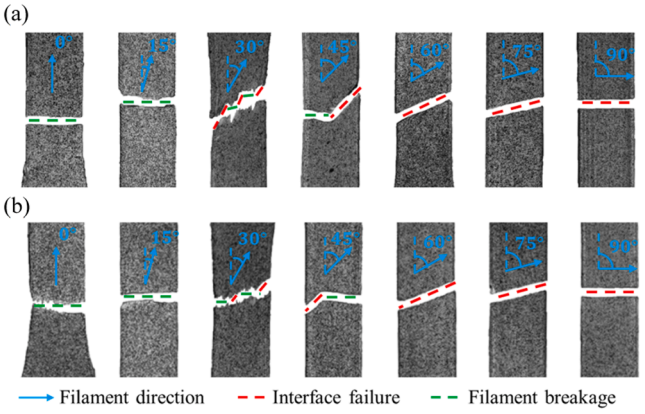

Fig. 7. Fractured samples in Plane 13 with (a) air gap = 0 mm and (b) air gap = -0.05 mm.

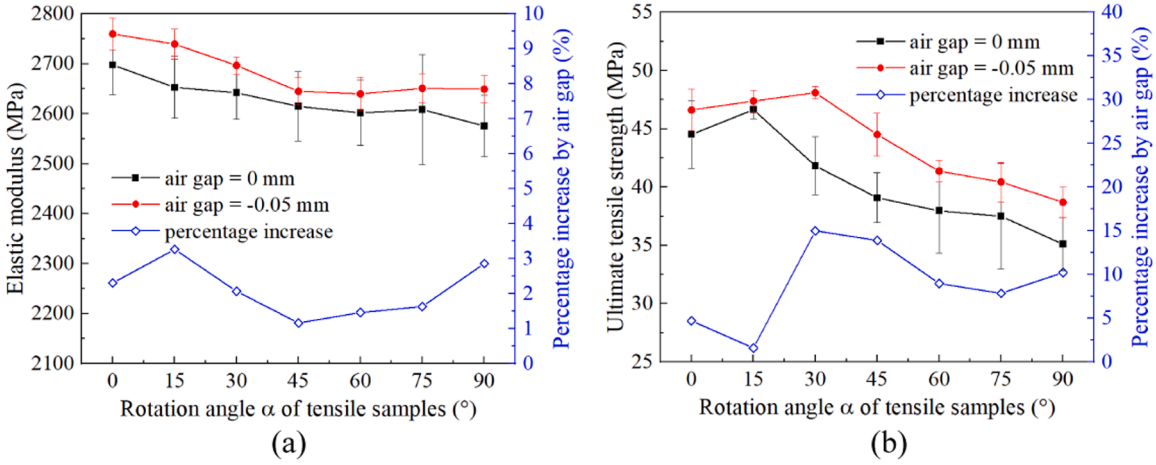

Fig. 6. Tensile results in Plane 12 (a) elastic modulus, and (b) ultimate tensile strength.

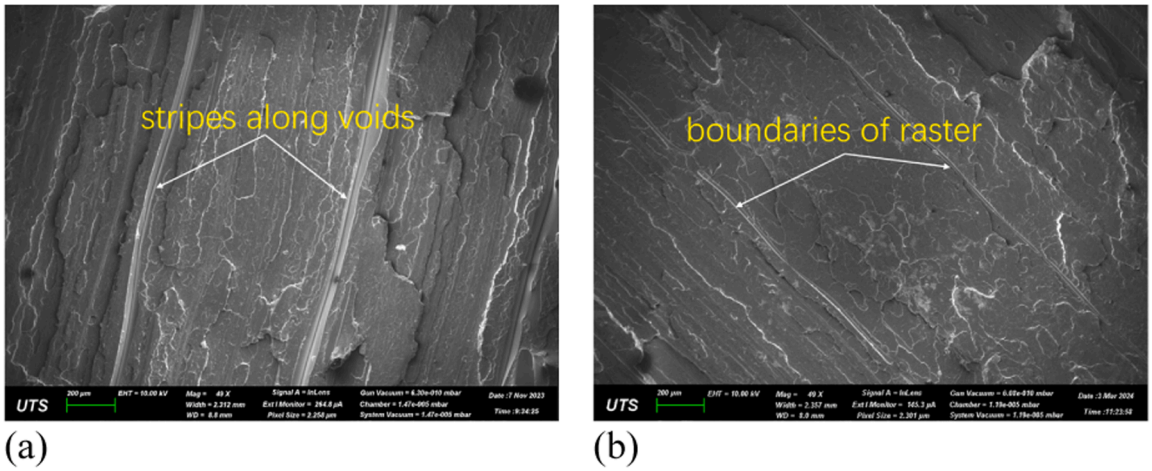

Fig. 8. SEM images of fracture surfaces in Plane 13 at 90° with (a) air gap = 0 mm, and (b) air gap = -0.05 mm.

SEM images in Fig. 8 show the interlayer failure of samples at 90°. In Fig. 8(a), the large width of the strips between voids, resulting in the voids in samples with air gap of 0 mm, decreased the bonding area of filament between different layers. By contrast, the width of strips along voids got smaller with the decreasing of air gap shown in Fig. 8(b) and indicated the boundaries of raster within layers. Although the enhancement by -0.05 mm, the increase of bonding strength was not enough to change the fracture modes of samples in Plane 13.

With the layer height of 0.2 mm, the samples in Plane 13 exhibited a smoother dimensional variation within the radius area compared with those in Plane 12. Nevertheless, the breakage of samples at 0° still occurred around the radius area. Fig. 9 presents the contour of the maximum principal strain ε_1 for samples at 0°. Strain localization was not apparent at a strain ratio of 2 % which corresponded to reaching the UTS. When ε_y reached 2.5 %, strain localization occurred at the end of fillet radius area as well as the supported side (left side) of the sample as depicted in Fig. 1(a). Contact with the support resulted in an uneven surface on the samples, contributing to the strain localization. Attributed to the smooth dimensional variation, failure was avoided before reaching the UTS in Plane 13 samples at 0°.

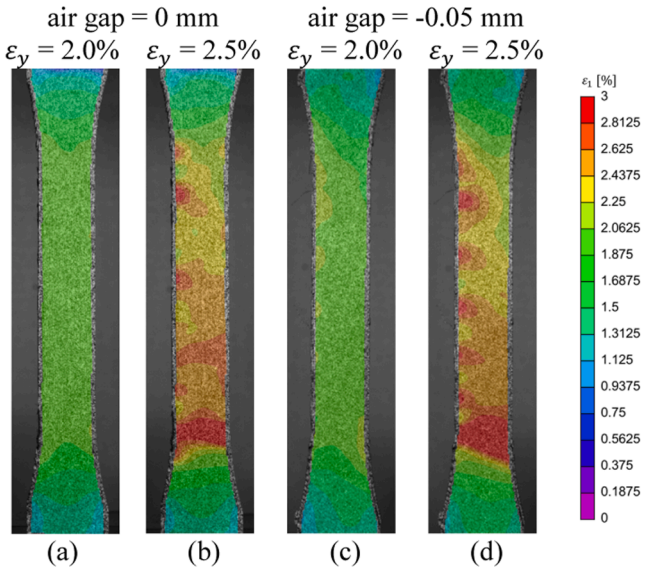

Fig. 9. Contour of maximum principal strain ε_1 for 0° samples at (a and b) 0 mm, and (c and d) -0.05 mm air gap, with ε_y at 2.0 % and 2.5 %.

3.2.2. *Tensile results with different air gaps*

The stress-strain curves of samples in Plane 13 were presented in Fig. 10. For rotation angles less than 45°, samples with air gap of 0 mm displayed plastic deformation before break. When the samples rotated from 60° to 90°, plasticity diminishes, accompanied by the transition in fracture mode from combined fracture to interface failure. Interestingly, samples with -0.05 mm air gap consistently demonstrated stages of plastic deformation, even when experiencing the interface failure mode. As evidenced by SEM images in Fig. 8(b), the interface failure of the sample with -0.05 mm air gap spanned across layers, as the fracture surface was not as smooth as that of the sample with 0 mm air gap.

The elastic modulus of samples obtained from the enlarged linear segment in Fig. 10 was presented in Fig. 11(a). The elastic modulus significantly decreased with the increase of rotation angles for air gap cases. The most substantial decrease in elastic modulus occurred in samples ranging from 0° to 45°. With 0 mm air gap, the maximum value was 2709 MPa at 0°, while the elastic modulus decreased to 2302 MPa at 45°. When the rotation angle exceeded 45°, the samples exhibited similar elastic modulus at around 2250 MPa. The -0.05 mm air gap enhanced the elastic modulus of samples in Plane 13, ranging from 1.25 % (at 75°) to 6.37 % (at 30°). The average increase in elastic modulus in Plane 13 is 3.1 %, which is slightly higher than that in Plane 12.

The UTS exhibited a decreasing trend as the rotation angle increased as shown in Fig. 11(b), influenced by interlayer bonding. For samples with 0 mm gap, the UTS underwent a significant reduction from 49.5 MPa at 0° to 29.4 MPa at 75°. Subsequently, it experienced a slight increase as the rotation angle further increased to 90°. The impact of air gap on UTS enhancement also varied among samples with different rotation angles. The improvement in sample at 0° can be considered negligible while the highest percentage increase was observed in samples at 75°, reaching 21.1 %. Hence, the −0.05 mm air gap increased the UTS by an average of 8.4 % in Plane 13. The enhancement by the negative air gap did not exhibit significant difference across different planes.

3.3. *Defect in samples in Plane 23*

For samples printed in Plane 23, the included angle between the filament and the tensile loading direction remains constant at 90°. The filaments were deposited along the thickness direction of the dog-bone samples which is only 4 mm in length. A noticeable defect in the form of ripples, as shown in Fig. 12(b), was observed in these samples. The extruded material did not distribute evenly, and the line width varied along the printing path, leading to the formation of ripples and the presence of voids between filaments. As demonstrated by Basile et al. [50], the ripple defect was caused by the pressure fluctuation in the

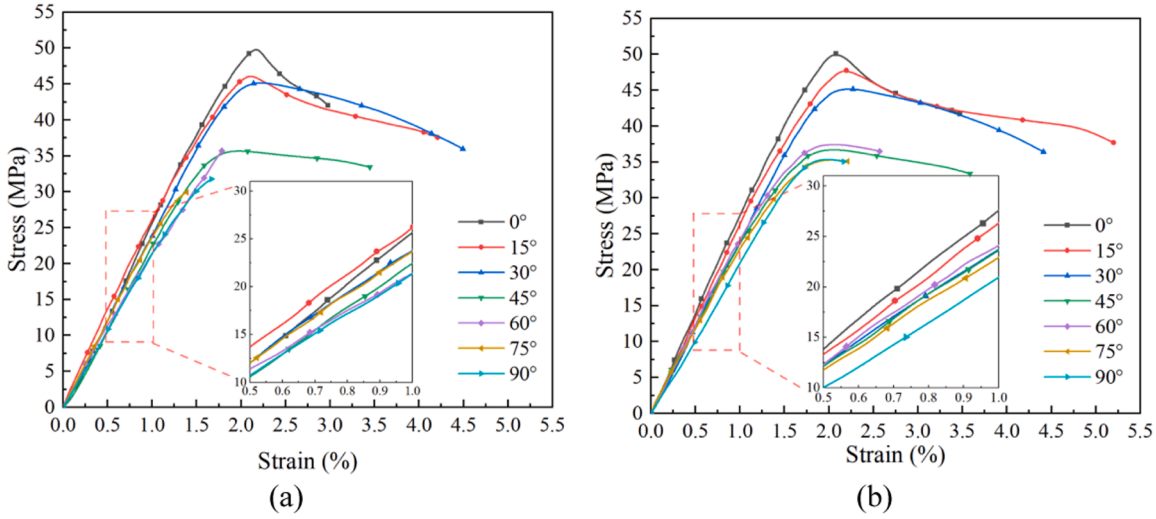

Fig. 10. Stress-strain curves of samples in Plane 13 with (a) air gap = 0 mm, and (b) air gap = -0.05 mm.

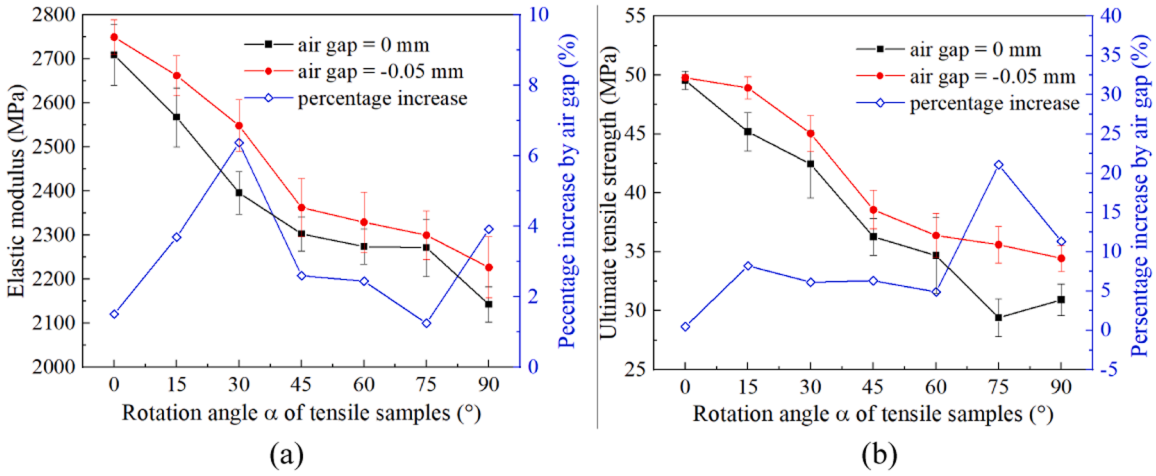

Fig. 11. Tensile results in Plane 13 (a) elastic modulus, and (b) ultimate tensile strength.

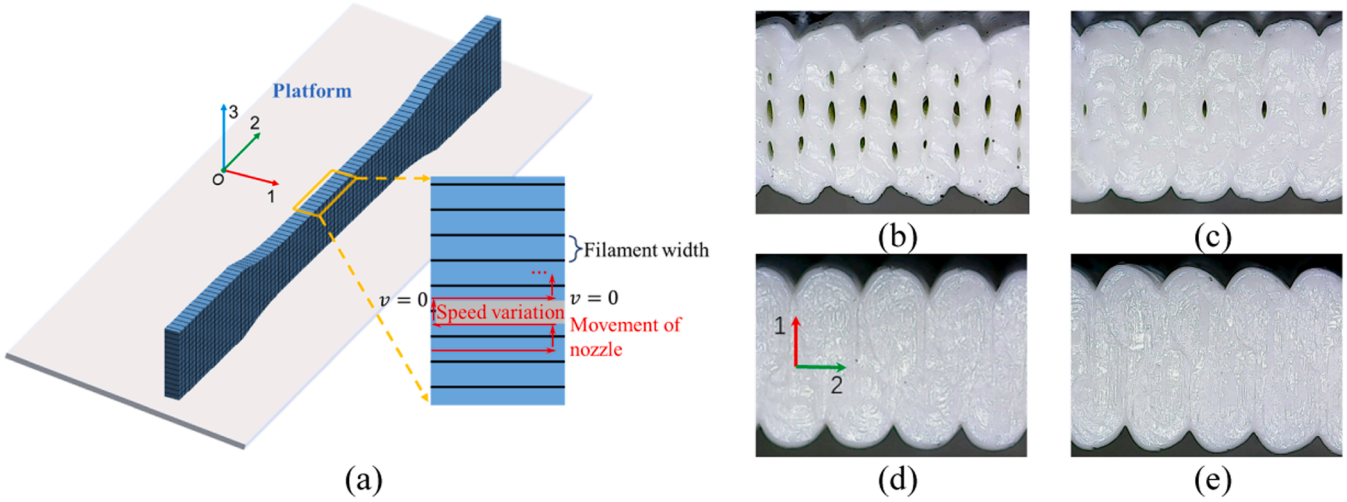

Fig. 12. (a) The diagram of nozzle movement during the deposition process; effect of air gap and printing speed on the microstructure of samples in Plane 23: (b) air gap = 0 mm, v_1 = 45 mm/s, (c) air gap = -0.05 mm, v_1 = 45 mm/s, (d) air gap = 0 mm/s, v_1 = 15 mm/s, and (e) air gap = -0.5 mm, v_1 = 15 mm/s.

extrusion chamber during the frequent change in motion direction.

Fig. 12(a) illustrates the nozzle movement during the deposition process. Initially, the nozzle moved along the thickness direction at a speed of 0 mm/s. Subsequently, it must accelerate to reach the printing speed of 45 mm/s as listed in Table 1. Upon arriving at the opposite end of the printing path, the nozzle's speed decelerates to 0 mm/s. Following this, the nozzle moves upward along the tensile direction of the samples to print the subsequent paths. This process repeats until the layer is completed. The frequent change in movement direction requires a continuous variation in speed, leading to fluctuations in the extrusion pressure, which adversely affects the precision of the volume flow rate of melted polymer [44,49]. The ripple defect is more prominent in short printing paths due to the higher frequency of speed variations. This explains why the ripples occurred in samples from Plane 23, whereas they were not observed in samples from other planes.

Fig. 12(b) to (e) show the microstructure of samples at 0° printed in Plane 23. With a 0 mm air gap and a printing speed of 45 mm/s, the UTS of samples in Fig. 12(b) was only 8.7 MPa. When the line spacing was reduced by introducing a -0.05 mm air gap, a portion of the pores was eliminated (Fig. 12(c)), consequently enhancing the UTS to 17.8 MPa. To mitigate the defect and enhance the bonding quality further, the printing speed was reduced from 45 mm/s to 15 mm/s. Samples with air gap of 0 mm and −0.05 mm were shown in Fig. 12(d) and (e). In these samples, no pores were observed between the filament, and the UTS was improved to 24.7 MPa and 30.3 MPa, respectively. It should be noted that the UTS of samples at 90° in Plane 12 with air gap of 0 mm and −0.05 mm, was 35.1 MPa and 38.2 MPa, respectively. Comparable strength should be achieved by the samples in Plane 23 as these samples examine the strength perpendicular to the filament. However, even the bonding quality was improved by reducing the printing speed, the UTS of samples in Plane 23 remained lower. It was inferred that the difference in UTS resulted from the stress concentration at the edges of the samples. Due to the ripple defect and stress concentration, the mechanical properties of samples printed in Plane 23 were unreliable for investigating the anisotropy of FDM materials.

4. Discussions

4.1. The applicability of orthotropic mechanical models

4.1.1. Model calibration and error assessment

Hill48 yield model and the elastic compliance matrix were calibrated employing the experimental results. Due to the sample defects in Plane 23, the experimental data in Plane 23 was unreliable for the calibration of the mechanical models, leading to an absence of shear strength, modulus, and Poisson's ratio within Plane 23. Hence, five orthotropic parameters and seven elastic parameters were determined and presented in Tables 3 and 4, respectively.

In order to evaluate the reliability of theoretical models in FDM printed PLA materials, the mean absolute percentage error (MAPE) is adopted as a criterion, which is

$$MAPE = \frac{1}{n}\sum_{i=1}^{n}\left|\frac{\widehat{y_i} - y_i}{y_i}\right| \tag{15}$$

where $\widehat{y_i}$ and y_i represent the experimental results and theoretical data from the calibrated models, and n is the number of samples in each plane. As six duplicated samples were fabricated at each rotation angle, n is 42 in Planes 12 and 13.

Table 3
The calibration results of Hill48 yield model.

Orthotropic parameters	Air gap 0 mm ($\times 10^{-4}$)	-0.05 mm ($\times 10^{-4}$)
F	7.008	5.383
G	3.602	2.985
H	0.799	1.195
M	10.235	8.970
N	7.664	5.757

Table 4
Independent parameters in the compliance matrix of FDM printed parts.

Independent parameters	Air gap 0 mm	-0.05 mm
E_1 (MPa)	2669	2785
E_2 (MPa)	2583	2649
E_3 (MPa)	2208	2251
ν_{12}	0.43	0.43
ν_{13}	0.37	0.40
G_{12} (MPa)	919	924
G_{31} (MPa)	844	868

Table 5
Statistical analysis of the prediction error.

Air gap (mm)	MAPE in UTS (%)		MAPE in elastic modulus (%)	
	Plane 12	Plane 13	Plane 12	Plane 13
0	4.8	5.2	2.1	2.3
-0.05	3.0	3.1	1.0	2.0

As shown in Table 5, both elastic modulus and strength of FDM samples in different planes were accurately predicted with an acceptable error. The error in prediction may result from the manufacturing uncertainties. Introducing a negative air gap reduced MAPE of prediction for both UTS and elastic modulus, attributing to the reduction of the printing uncertainties, such as the deposition shape and position precision. Specifically, with a 0 mm air gap, the MAPE in elastic modulus was 2.1 % for samples in Plane 12 and 2.3 % for Plane 13, respectively. It decreased to 1.0 % and 2.0 % with a -0.05 mm air gap. Besides, the predicted tensile strength from calibrated Hill48 model exhibited MAPE of 4.8 % and 5.2 % with the experimental results in Plane 12 and Plane 13. It decreased to 3.0 % and 3.1 % when air gap was -0.05 mm.

Fig. 13 compares the elastic modulus obtained from the compliance matrix with the experimental results. It was observed from Fig. 13(a) that deviations occurred in the Plane 13 samples when rotation angles were greater than 60°. With a negative air gap as shown in Fig. 13(b), the samples at 75° and 90° still exhibit higher discrepancy with prediction curves. The prediction curves in Plane 13 tend to underestimate the elastic modulus at 60° and 75° and overestimate it at 90°. In contrast, the experimental data in Plane 12 did not show significant deviation from the calibrated curves at all rotation angles. Fig. 14 presents a comparison between the theoretical strengths obtained from the calibrated Hill48 model and the experimental results. In the case of 0 mm air gap shown in Fig. 14(a), the deviation from the prediction curves also occurred at 60° and 75° in both Plane 12 and 13. When the air gap decreased to -0.05 mm in Fig. 14(b), the experimental data closely follow the prediction curves, without noticeable deviations. Overall, the compliance matrix and calibrated Hill48 model demonstrate a great fit to the experimental data.

4.1.2. Discussion of the orthotropy characterized by Hill48 yield model

The calibration of Hill48 yield model only considered the strength of tensile samples under states of plane stress. To examine the orthotropic behavior of FDM material, the yield surfaces were discussed in this section. The anisotropic yield surface represented by Hill48 yield model was six-dimensional hypersurfaces in the space of stress components. To offer a clear understanding, two-dimensional yield loci were provided as a graphical representation by fixing the other four stress components.

The range of values for the fixed stress components were determined by the uniaxial yield strengths and shear strengths. In the orthotropic Hill48 yield model, the uniaxial tensile strengths of FDM materials in the orthotropic principal directions were defined as T_1, T_2, and T_3, respec-

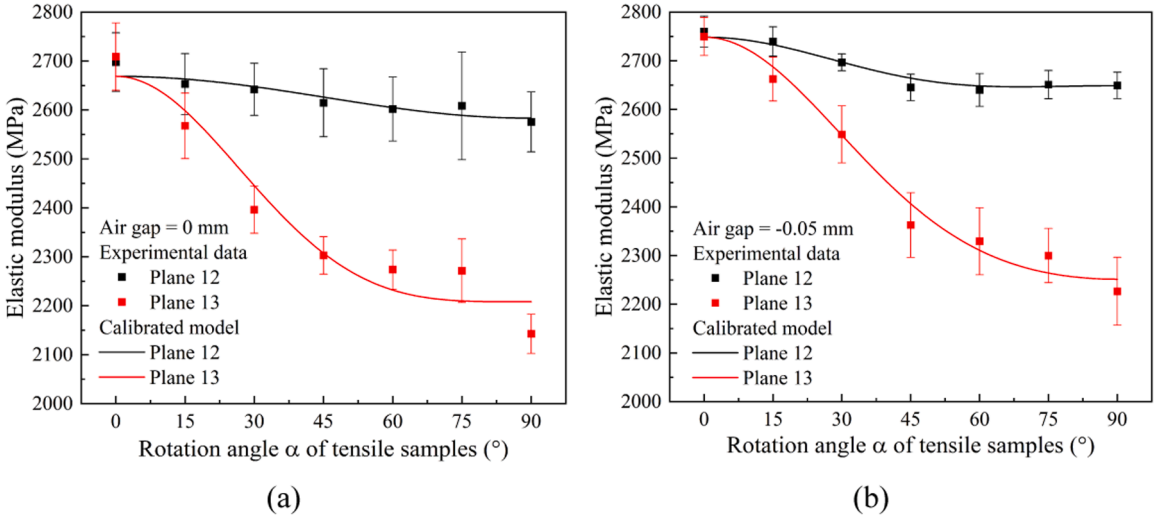

Fig. 13. Comparison between the results from the calibrated compliance matrix and experimental data for (a) air gap = 0 mm, and (b) air gap = -0.05 mm.

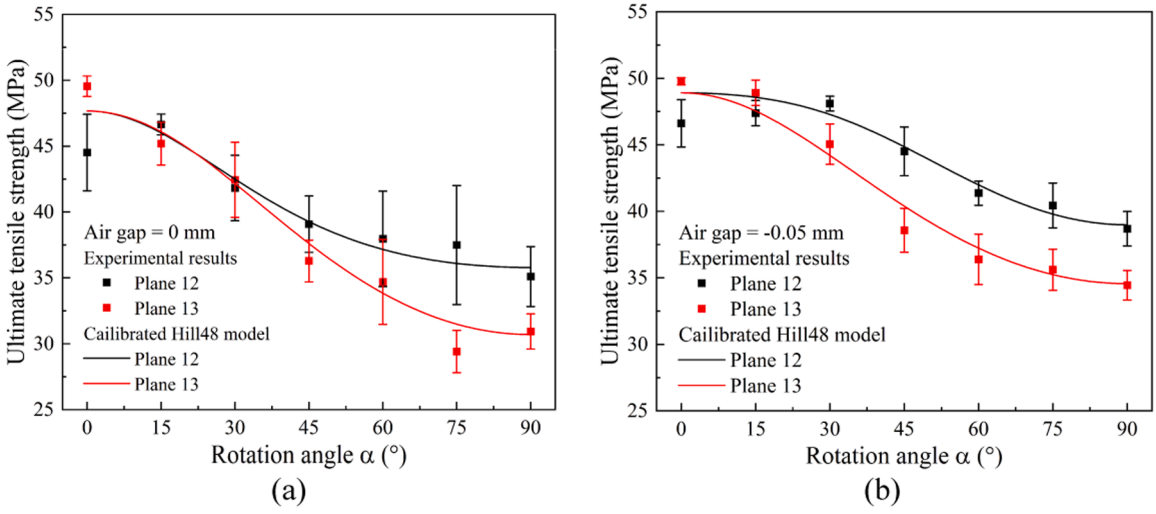

Fig. 14. Comparison between the results from the calibrated Hill48 models and experimental data for (a) air gap = 0 mm, and (b) air gap = -0.05 mm.

tively. The shear strengths were defined as S_{12} and S_{31} with respect to the orthotropic principal axes. These strengths were provided as follows:

$$T_1 = \frac{1}{\sqrt{G+H}},\ T_2 = \frac{1}{\sqrt{F+H}},\ T_3 = \frac{1}{\sqrt{F+G}},\ S_{12} = \frac{1}{\sqrt{2N}},\ S_{31} = \frac{1}{\sqrt{2M}} \tag{16}$$

Hence, the theoretical strength of FDM materials, derived from the calibrated Hill48 model, was obtained as presented in Table 6.

Figs. 15(a) to (c) present the yield surfaces of Hill48 orthotropic model plotted on the $\sigma_{11} - \sigma_{22}$, $\sigma_{11} - \sigma_{33}$ and $\sigma_{22} - \sigma_{33}$ spaces with different values of another normal stress, assuming no shear stresses, i.e., $\sigma_{12} = \sigma_{31} = \sigma_{23} = 0$. In Fig. 15(a), the yield surfaces were ellipses intersecting the horizontal axis at $\pm T_1$ and the vertical axis at $\pm T_2$ when $\sigma_{33} = 0$. Notably, the yield surface of sample with air gap of 0 mm consistently lied within the yield surface of sample with a -0.05 mm air gap contributing to the enhancement performance. The center of the ellipses was presented by (σ_{33}, σ_{33}). The Hill48 yield model is an extension of the von Mises yield model to take into account the material anisotropy. It is a pressure insensitive model with an axis of symmetry defined by $\sigma_{11} = \sigma_{22} = \sigma_{33}$. Consequently, the yield surfaces are translated along the $\sigma_{22} = \sigma_{11}$ direction when σ_{33} increases, while maintaining the same shape. It is important to note that the applicability of Hill48 yield model is constrained within specific ranges of hydrostatic pressure, limited by the assumption of hydrostatic pressure independence inherited from the von Mises yield model.

Table 6
Strength of materials from Hill48 yield model.

Strength (MPa)	Air gap	
	0 mm	-0.05 mm
T_1	47.7	48.8
T_2	35.8	38.9
T_3	30.7	34.1
S_{12}	25.5	29.4
S_{31}	22.1	23.6

The yield surfaces in Fig. 15(a) to (c) exhibited varying extents of protrusion within the first quadrant, a characteristic that relied on the ratios of strengths along different principal axes. In the $\sigma_{11} - \sigma_{22}$ space, the eccentricity was governed by the ratios of $\frac{\sigma_{33}}{\sigma_{11}}$ and $\frac{\sigma_{33}}{\sigma_{22}}$. The larger the ratios, the more pronounced the anisotropy and the protrusion. With $\sigma_{11} > \sigma_{22} > \sigma_{33}$ in the calibrated model, the protrusion became more noticeable from Fig. 15(a) to (c). This indicates that under the plane stress state, the normal stress of σ_{22} and σ_{33} can exceed the strength that is achieved under the uniaxial tension state.

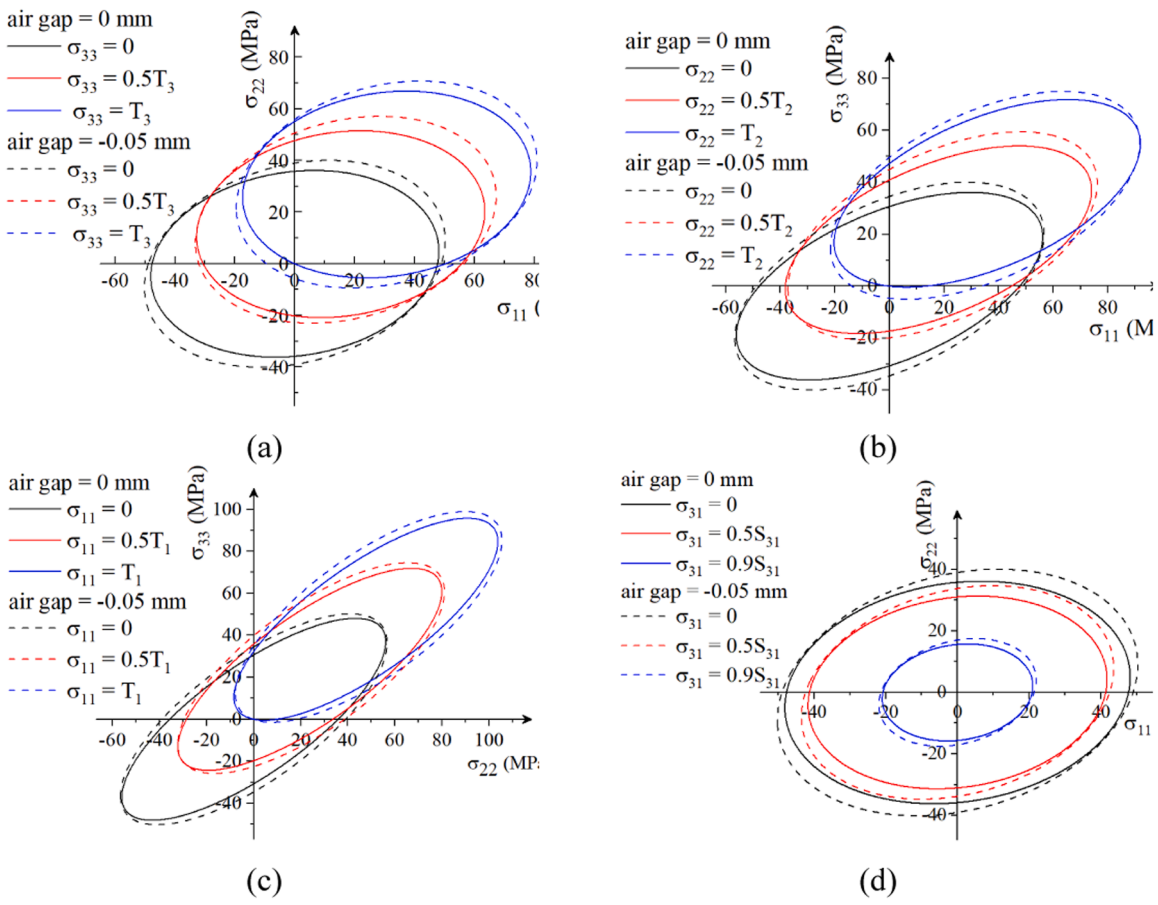

Fig. 15. The yield surfaces of calibrated Hill48 model on the (a) $\sigma_{11} - \sigma_{22}$, (b) $\sigma_{11} - \sigma_{33}$ and (c) $\sigma_{22} - \sigma_{33}$ spaces when $\sigma_{12} = \sigma_{31} = \sigma_{23} = 0$ and (d) on the $\sigma_{11} - \sigma_{22}$ space when $\sigma_{33} = \sigma_{12} = \sigma_{23} = 0$.

Fig. 15(d) illustrates the yield surface in the $\sigma_{11} - \sigma_{22}$ space when $\sigma_{33} = \sigma_{12} = \sigma_{23} = 0$ to specifically examine the impact of shear stress. Evidently, an increase in shear stress shrank the yield surface proportionally in all directions while preserving shape. As the shear stress reached its yield limitation, the $\sigma_{11} - \sigma_{22}$ space degenerated to a point at (0, 0).

The Hill48 yield model has been widely used for metal materials owing to its simplicity and direct significance of the coefficients. However, it should be noted that the Hill48 yield model exhibits limitations in predicting some particular phenomena [51]. As demonstrated by Mu et al. [52], it can only effectively predict several inherent forms of the uniaxial tensile yield stress and Lankford coefficients (r-value). It cannot represent 'anomalous behavior' where $r < 1$ and biaxial yield stress is lower than uniaxial yield stress and 'second anomalous behavior' where $\frac{r_0}{r_{90}} > 0$ and $\frac{\sigma_0}{\sigma_{90}} < 1$ (or vice-versa). This study focused on the strength of FDM printed materials and neglected the calculation of r-value, which may lead to inaccurate predictions of plastic deformations.

4.2. Discussion on the orthotropic behavior of FDM materials

4.2.1. Orthotropy in stiffness of FDM materials

When comparing tensile samples in different planes, it was observed that the maximum elastic modulus values were almost the same, measuring 2700 MPa (with a 0 mm air gap) and 2750 MPa (with a -0.05 mm air gap), both achieved at a rotation angle of 0°. However, the minimum values for samples in different planes showed significant differences. When the air gap was 0 mm, the minimum elastic modulus in plane 12 was 2575 MPa, whereas in plane 13, it was only 2142 MPa. The anisotropy of elastic moduli in Plane 13 was more pronounced than in Plane 12. Despite the enhancement in elastic modulus with a -0.05 mm air gap, the modulus difference within the plane remained unchanged. The FDM samples exhibited orthotropic elasticity in three-dimensional space.

According to the theory of polymer physics [53], the mechanical properties of polymers are highly dependent on polymer chain segment orientation. Specifically, the stiffness along the polymer chains is higher than that perpendicular to them. The orientation of chains is created when a molten polymer is subjected to external mechanical forces. The alignment of chains can be maintained permanently through rapid cooling, solidifying the oriented molten polymer. Chain orientation or alignment is a common occurrence in polymers. In the injection molding process, the polymer chains naturally align in the direction of flow. The core of an injection-molded specimen is typically unoriented due to the relaxation process [54], whereas the material near the surface remains oriented as it makes contact with the cooler mold surfaces. Chain orientation induces anisotropic properties unless the intrinsic properties of the chains are isotropic.

In the FDM process, the molten polymer material experiences shear and stretching forces while being extruded through the nozzle. These forces induce the orientation or alignment of polymer chains in the direction of filament [55,56]. Typically, FDM printers are equipped with fans to cool the molten material after extrusion. This ensures rapid solidification of material to maintain a stable shape and prevents undesired deformation. As a result, the orientation of chains is established and solidified during the extrusion and subsequent solidification processes. Due to the difference in shear rate along the radius of nozzle, the molecular chains exhibit a higher degree of orientation within a certain depth from the surface of the extruded filament [57]. As the depth

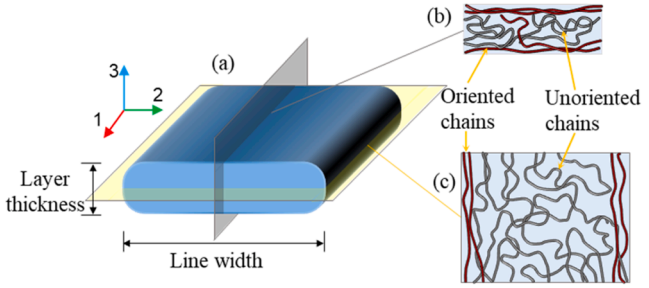

Fig. 16. Chain orientation model of FDM filament (a) the deposited filament, (b) vertical profile of filament in Plane 13, (c) horizontal profile of filament in Plane 12.

increases, the orientation gradually diminishes, as shown in Fig. 16. As listed in Table 1, the extruded filament had a width of 0.8 mm and a thickness of 0.2 mm. The percentage of areas exhibiting chain alignment in Plane 12 samples (except the sample at 0°) was considerably lower than those in Plane 13. For example, at a rotation angle of 90°, the proportion of chain orientation regions in Plane 13 samples was approximately 4 times higher than that observed in Plane 12 samples. Hence, the anisotropy in elastic modulus of samples in Plane 13 was more pronounced which highlights the impact of chain orientation.

4.2.2. Orthotropy in strength of FDM materials

FDM printed PLA materials demonstrated noticeable strength anisotropy in both Plane 12 and Plane 13 with respect to the rotation of filament direction, accompanied by a transition in fracture mode. Due to the premature breakage of filament in sample at 0° in Plane 12, the maximum UTS value obtained at 0° in Plane 13 slightly exceeded that in Plane 12. However, the minimum value in Plane 12 was higher than that in Plane 13. When the air gap was 0 mm, the minimum value was 35.1 MPa in Plane 12, exceeding that of samples in Plane 13 (30.9 MPa). The differences between the maximum and the minimum value of tensile strength are 20.1 MPa in Plane 13 and 11.5 MPa in Plane 12, respectively. When the air gap was -0.05 mm, the differences reduced to 15.3 and 8.0 MPa in these two Planes. The larger difference in Plane 13 suggests that the impact of interlayer bonding on strength was more pronounced than the filament-to-filament bonding within layers.

Sun et al. [58] outlined the bonding formation process between adjacent filaments as comprising three stages: (1) surface contacting, (2) neck formation, and (3) molecular diffusion and randomization of the polymer chains across the interface. During the surface contacting and neck formation stage, the bonding surfaces are created, serving as the foundation for strength development. The process parameters that affect the microstructure and solidity of printed parts play a crucial role in this process, such as layer thickness, line width, air gap, infill percentage, and others. In the third stage, the molecular chains move across the interface according to de Gennes' reptation model [54]. Wool and O'Connor [59] developed a crack healing theory based on the reptation model to predict the mechancial properties of cracked polymer material after healing. In their theory, the interface bonding strength is determined by the quantity of polymer chains and their migration beyond the initial interface into the adjoining side. When two contacted polymeric interfaces are heated to a temperature above their glass transition temperature or melting temperature, the interpenetration distance χ of moleculars increases with healing time t and reaches its maximum χ_∞ at reptation time t_∞. The bond strength depends on the interpenetration distance χ. When the interpenetration distance reaches its maximum, the maximum bond strength σ_∞ can be achieved. The interface disappears and is indistinguishable from the bulk [60]. The interpenetration distance χ depends on the healing temperature and the duration of molecular diffusion. Hence, before degradation occurs in polymer materials, the higher the temperature or the longer the healing time, the greater the strength of the bonding surface.

In FDM, adjacent filaments within layers are sequentially deposited, establishing filament-to-filament bonds within a short period of time. A shorter deposition interval results in a smaller temperature gradient. Comparatively, filaments in different layers experience a longer deposition interval, as each subsequent layer is printed after the completion of the previous one. When a filament is deposited, its previous layer may have undergone cooling [19,61]. In that case, molecular diffusion between the layers is restricted due to a higher temperature gradient, resulting in insufficient interpenetration of chains across the bonding surface and lower bonding strength [62]. Hence, the interlayer bonding induced more pronounced anisotropy in UTS.

The size of samples, the quantity of samples printed in one batch, and the printing speed influence the cooling time between layers. Increasing the printing speed can reduce the time interval for filament deposition, which helps enhance molecular diffusion and thus leads to higher bond strength. Additionally, printing efficiency depends on the printing speed. However, as observed in Section 3.3, a high printing speed can result in bonding defects, compromising printing quality. Therefore, when optimizing printing speed, it is important to consider its comprehensive impacts on bond strength, printing quality, and printing efficiency.

The presence of a -0.05 mm air gap improved interface bonding by eliminating pores and densifying the microstructure. However, the difference between the maximum and minimum values was 15.3 MPa in Plane 13, which was still higher than that observed in Plane 12 (9.4 MPa). The lower UTS of samples with interface failure resulted primarily from the insufficient bonding strength between filaments. These findings suggest that the influence of interface bonding cannot be eliminated solely by filament overlap. The negative air gap ensures adequate interface contact but does not achieve sufficient interpenetration of molecular chains.

5. Conclusions

In this study, the mechanical anisotropy of FDM printed PLA material and the impact of air gap are investigated by testing dog-bone samples that were fabricated in three-dimensional space. Two air gap levels (0 mm and -0.05 mm) and seven loading directions (0° to 90° at 15° interval) were examined in each orthotropic plane. The following conclusions are drawn:

FDM printed PLA materials exhibited orthotropic behavior in three-dimensional space under specific printing conditions. The anisotropy induced by interlayer bond was more pronounced than that resulting from filament-to-filament bond within layer. The air gap of -0.05 mm significantly reduced voids, and hence enhanced both stiffness and strength. Its enhancement effect on intra-layer mechanical performance was more pronounced than on interlayer bonding, as demonstrated by the improved strength and the transition of fracture modes.

However, the negative air gap cannot eliminate the orthotropic characteristics of the printed PLA material. The decrease in voids resulting from the negative air gap indicates that the orthotropy in stiffness was primarily dominated by the orientation of molecular chains and the interface bonding strength was governed by the molecular chain diffusion. Therefore, the difference between the dimension of layer thickness and line width, as well as the rapid cooling after extrusion emerge as influential factors in determining the mechanical properties.

Pressure fluctuations accompanying rapid changes in printing speed induce notable ripple defects in Plane 23 samples. The negative air gap narrows the distance of filaments, contributing to mitigating the defect. Fundamentally, reducing the printing speed decreased the pressure fluctuations, effectively preventing the occurrence of this defect.

Orthotropic models demonstrate promise in accurately characterizing the mechanical properties of FDM printed materials compared to simplified transversely isotropic models. The calibrated Hill48 yield model and elastic compliance model show great agreement with

experimental data, affirming their suitability for describing the orthotropic properties of FDM printed materials.

This study provided a comprehensive investigation into the orthotropy and the influence of air gap on the tensile properties. While introducing a negative air gap is effective for enhancing stiffness and strength, it does not eliminate mechanical anisotropy. To reduce anisotropy, the focus can be on improving molecular chain diffusion and reduce chain orientation. This can be achieved by optimizing the temperature-related process parameters to extend the heal time and reduce cooling rate. If aiming to eliminating the mechanical anisotropy, further investigation can be conducted considering the effects of temperature-related parameters based on a proper negative air gap.

CRediT authorship contribution statement

Meiyu Li: Methodology, Software, Data curation, Visualization, Writing – original draft. **Yanan Xu:** Investigation, Data curation, Writing – review & editing. **Jianguang Fang:** Conceptualization, Methodology, Writing – review & editing, Project administration, Funding acquisition, Supervision.

Declaration of competing interest

The authors declare that they have no known competing financial interests or personal relationships that could have appeared to influence the work reported in this paper.

Acknowledgments

The support from the Australian Research Council (ARC) Discovery scheme (DP190103752) is acknowledged. The first author is a recipient of the FEIT Scholarship and IRS Scholarship at the University of Technology Sydney. The last author is a recipient of the ARC Discovery Early Career Research Award (DE210101676).

References

[1] S. Aghajani, C. Wu, Q. Li, J. Fang, Additively manufactured composite lattices: a state-of-the-art review on fabrications, architectures, constituent materials, mechanical properties, and future directions, Thin-Walled Struct. 197 (2023) 111539, https://doi.org/10.1016/j.tws.2023.111539.

[2] M. Tunay, Bending behavior of 3D printed sandwich structures with different core geometries and thermal aging durations, Thin-Walled Struct. 194 (2024) 111329, https://doi.org/10.1016/j.tws.2023.111329.

[3] H. Sadaghian, S. Khalilzadehtabrizi, M. Farzam, S. Dehghan, Behavior of 3D-printed polymers under monotonic torsion – a database of 15 different materials, Addit. Manuf. 60 (2022) 103251, https://doi.org/10.1016/j.addma.2022.103251, 2022.

[4] B. Herath, et al., Mechanical and geometrical study of 3D printed Voronoi scaffold design for large bone defects, Mater. Des. 212 (2021) 110224, https://doi.org/10.1016/j.matdes.2021.110224.

[5] M. Lay, N.L.N. Thajudin, Z.A.A. Hamid, A. Rusli, M.K. Abdullah, R.K. Shuib, Comparison of physical and mechanical properties of PLA, ABS and nylon 6 fabricated using fused deposition modeling and injection molding, Compos. Part B Eng. 176 (2019) 107341, https://doi.org/10.1016/j.compositesb.2019.107341.

[6] T.J. Coogan, D.O. Kazmer, Prediction of interlayer strength in material extrusion additive manufacturing, Addit. Manuf. 35 (2020) 101368, https://doi.org/10.1016/j.addma.2020.101368.

[7] S.R. Rajpurohit, H.K. Dave, Analysis of tensile strength of a fused filament fabricated PLA part using an open-source 3D printer, Adv. Manuf. 6 (2018) 430–441, https://doi.org/10.1007/s40436-018-0237-6.

[8] T. Yao, J. Ye, Z. Deng, K. Zhang, Y. Ma, H. Ouyang, Tensile failure strength and separation angle of FDM 3D printing PLA material: experimental and theoretical analyses, Compos. Part B Eng. 188 (2020) 107894, https://doi.org/10.1016/j.compositesb.2020.107894.

[9] M. Dawoud, I. Taha, S.J. Ebeid, Mechanical behaviour of ABS: an experimental study using FDM and injection moulding techniques, J. Manuf. Process. 21 (2016) 39–45, https://doi.org/10.1016/j.jmapro.2015.11.002.

[10] S. Ding, B. Zou, P. Wang, H. Ding, Effects of nozzle temperature and building orientation on mechanical properties and microstructure of PEEK and PEI printed by 3D-FDM, Polym. Test. 78 (2019) 105948, https://doi.org/10.1016/j.polymertesting.2019.105948.

[11] M. Jimenez-Martinez, J. Varela-Soriano, J.J.R. Carreón, S.G. Torres-Cedillo, Mechanical fatigue of PLA in additive manufacturing, Eng. Fail. Anal. 149 (2023) 107273, https://doi.org/10.1016/j.engfailanal.2023.107273.

[12] R. Ahmadi, D. D'Andrea, D. Santonocito, Fatigue assessment of 3D-printed porous PLA-based scaffold structures by thermographic methods, IOP Conf. Ser. Mater. Sci. Eng. 1275 (2023) 012002, https://doi.org/10.1088/1757-899x/1275/1/012002.

[13] K. Chen, F. Yang, C. Yao, T. Liu, H. Jiang, Single material FDM printed nacre-like composite structure with high fracture resistance: utilizing interface as soft phase, Compos. Commun. 42 (2023) 101682, https://doi.org/10.1016/j.coco.2023.101682.

[14] M.A. Caminero, J.M. Chacón, I. García-Moreno, G.P. Rodríguez, Impact damage resistance of 3D printed continuous fibre reinforced thermoplastic composites using fused deposition modelling, Compos. Part B Eng. 148 (2018) 93–103, https://doi.org/10.1016/j.compositesb.2018.04.054.

[15] D. Garcia-Gonzalez, A. Rusinek, T. Jankowiak, A. Arias, Mechanical impact behavior of polyether-ether-ketone (PEEK), Compos. Struct. 124 (2015) 88–99, https://doi.org/10.1016/j.compstruct.2014.12.061.

[16] M.R. Khosravani, S. Rezaei, S. Faroughi, T. Reinicke, Experimental and numerical investigations of the fracture in 3D-printed open-hole plates, Theor. Appl. Fract. Mech. 121 (2022) 103543, https://doi.org/10.1016/j.tafmec.2022.103543.

[17] O. Lampron, A. Lingua, D. Therriault, M. Lévesque, Characterization of the non-isotropic tensile and fracture behavior of unidirectional polylactic acid parts manufactured by material extrusion, Addit. Manuf. 61 (2023) 103369, https://doi.org/10.1016/j.addma.2022.103369.

[18] M.R. Khosravani, S. Rezaei, H. Ruan, T. Reinicke, Fracture behavior of anisotropic 3D-printed parts: experiments and numerical simulations, J. Mater. Res. Technol. 19 (2022) 1260–1270, https://doi.org/10.1016/j.jmrt.2022.05.068.

[19] V.E. Kuznetsov, A.N. Solonin, A. Tavitov, O. Urzhumtsev, A. Vakulik, Increasing strength of FFF three-dimensional printed parts by influencing on temperature-related parameters of the process, Rapid Prototyp. J. 26 (2020) 107–121, https://doi.org/10.1108/RPJ-01-2019-0017.

[20] T.Q. Tran, F.L. Ng, J.T.Y. Kai, S. Feih, M.L.S. Nai, Tensile strength enhancement of fused filament fabrication printed parts: a review of process improvement approaches and respective impact, Addit. Manuf. 54 (2022) 102724, https://doi.org/10.1016/j.addma.2022.102724.

[21] J.A. Afonso, J.L. Alves, G. Caldas, B.P. Gouveia, L. Santana, J. Belinha, Influence of 3D printing process parameters on the mechanical properties and mass of PLA parts and predictive models, Rapid Prototyp. J. 27 (2021) 487–495, https://doi.org/10.1108/RPJ-03-2020-0043.

[22] M. Algarni, The influence of raster angle and moisture content on the mechanical properties of pla parts produced by fused deposition modeling, Polymers (Basel) 13 (2021) 1–12, https://doi.org/10.3390/polym13020237.

[23] X. Gao, S. Qi, X. Kuang, Y. Su, J. Li, D. Wang, Fused filament fabrication of polymer materials: a review of interlayer bond, Addit. Manuf. 37 (2021) 101658, https://doi.org/10.1016/j.addma.2020.101658.

[24] P.G. De Gennes, Reptation of a polymer chain in the presence of fixed obstacles, J. Chem. Phys. 2 (1971) 35–42, https://doi.org/10.1142/9789812564849_0015.

[25] S.F. Edwards, The statistical mechanics of polymerized material, Proc. Phys. Soc. 92 (1967) 9–16, https://doi.org/10.1088/0370-1328/92/1/303.

[26] J. Allum, A. Moetazedian, A. Gleadall, V.V. Silberschmidt, Interlayer bonding has bulk-material strength in extrusion additive manufacturing: new understanding of anisotropy, Addit. Manuf. 34 (2020) 101297, https://doi.org/10.1016/j.addma.2020.101297.

[27] D. Xu, J.F. Agassant, F. Pigeonneau, Dimensions of the deposited strand in the material extrusion process: experimental and numerical investigations, Addit. Manuf. 59 (2022) 103107, https://doi.org/10.1016/j.addma.2022.103107.

[28] L. Fang, Y. Yan, O. Agarwal, J.E. Seppala, K.J. Hemker, S.H. Kang, Processing-structure-property relationships of bisphenol-A-polycarbonate samples prepared by fused filament fabrication, Addit. Manuf. 35 (2020) 101285, https://doi.org/10.1016/j.addma.2020.101285.

[29] J. Allum, A. Moetazedian, A. Gleadall, V.V. Silberschmidt, Interlayer bonding has bulk-material strength in extrusion additive manufacturing: new understanding of anisotropy, Addit. Manuf. 34 (2020) 101297, https://doi.org/10.1016/j.addma.2020.101297.

[30] J. Allum, A. Gleadall, V.V. Silberschmidt, Fracture of 3D-printed micro-tensile specimens: filament-scale geometry-induced anisotropy, Procedia Struct. Integr. 28 (2020) 591–601, https://doi.org/10.1016/j.prostr.2020.10.069.

[31] S.A. Tronvoll, T. Welo, C.W. Elverum, The effects of voids on structural properties of fused deposition modelled parts: a probabilistic approach, Int. J. Adv. Manuf. Technol. 97 (2018) 3607–3618, https://doi.org/10.1007/s00170-018-2148-x.

[32] G. Alaimo, S. Marconi, L. Costato, F. Auricchio, Influence of meso-structure and chemical composition on FDM 3D-printed parts, Compos. Part B Eng. 113 (2017) 371–380, https://doi.org/10.1016/j.compositesb.2017.01.019.

[33] A. Özen, B.E. Abali, C. Völlmecke, J. Gerstel, D. Auhl, Exploring the role of manufacturing parameters on microstructure and mechanical properties in fused deposition modeling (FDM) using PETG, Appl. Compos. Mater. 28 (2021) 1799–1828, https://doi.org/10.1007/s10443-021-09940-9.

[34] J.F. Rodríguez, J.P. Thomas, J.E. Renaud, Design of fused-deposition ABS components for stiffness and strength, J. Mech. Des. 125 (2003) 545–551, https://doi.org/10.1115/1.1582499.

[35] R. Zou, et al., Isotropic and anisotropic elasticity and yielding of 3D printed material, Compos. Part B Eng. 99 (2016) 506–513, https://doi.org/10.1016/j.compositesb.2016.06.009.

[36] A. Rahmati, M. Heidari-Rarani, L. Lessard, A novel conservative failure model for the fused deposition modeling of polylactic acid specimens, Addit. Manuf. 48 (2021) 102460, https://doi.org/10.1016/j.addma.2021.102460.

[37] P. Li, J. Yvonnet, C. Combescure, H. Makich, M. Nouari, Anisotropic elastoplastic phase field fracture modeling of 3D printed materials, Comput. Methods Appl. Mech. Eng. 386 (2021) 114086, https://doi.org/10.1016/j.cma.2021.114086.
[38] J.M. Chacón, M.A. Caminero, E. García-Plaza, P.J. Núñez, Additive manufacturing of PLA structures using fused deposition modelling: effect of process parameters on mechanical properties and their optimal selection, Mater. Des. 124 (2017) 143–157, https://doi.org/10.1016/j.matdes.2017.03.065.
[39] R.T.L. Ferreira, I.C. Amatte, T.A. Dutra, D. Bürger, Experimental characterization and micrography of 3D printed PLA and PLA reinforced with short carbon fibers, Compos. Part B Eng. 124 (2017) 88–100, https://doi.org/10.1016/j.compositesb.2017.05.013.
[40] S.J. Park, S.J. Park, Y. Son, I.H. Ahn, Reducing anisotropy of a part fabricated by material extrusion via warm isostatic pressure (WIP) process, Addit. Manuf. 55 (2022) 102841, https://doi.org/10.1016/j.addma.2022.102841.
[41] S.H. Ahn, M. Montero, D. Odell, S. Roundy, P.K. Wright, Anisotropic material properties of fused deposition modeling ABS, Rapid Prototyp. J., 8 (2002) 248–257, https://doi.org/10.1108/13552540210441166.
[42] Ultimaker Cura 4.12.1. https://ultimaker.com/software/ultimaker-cura/.
[43] C. Duty, et al., What makes a material printable? A viscoelastic model for extrusion-based 3D printing of polymers, J. Manuf. Process. 35 (2018) 526–537, https://doi.org/10.1016/j.jmapro.2018.08.008.
[44] P. Wang, B. Zou, H. Xiao, S. Ding, C. Huang, Effects of printing parameters of fused deposition modeling on mechanical properties, surface quality, and microstructure of PEEK, J. Mater. Process. Technol. 271 (2019) 62–74, https://doi.org/10.1016/j.jmatprotec.2019.03.016.
[45] P. Geng, et al., Effects of extrusion speed and printing speed on the 3D printing stability of extruded PEEK filament, J. Manuf. Process. 37 (2018) 266–273, https://doi.org/10.1016/j.jmapro.2018.11.023.
[46] S. Bakrani Balani, F. Chabert, V. Nassiet, A. Cantarel, Influence of printing parameters on the stability of deposited beads in fused filament fabrication of poly (lactic) acid, Addit. Manuf. 25 (2019) 112–121, https://doi.org/10.1016/j.addma.2018.10.012.
[47] Y. Zhao, Y. Chen, Y. Zhou, Novel mechanical models of tensile strength and elastic property of FDM AM PLA materials: experimental and theoretical analyses, Mater. Des. 181 (2019) 108089, https://doi.org/10.1016/j.matdes.2019.108089.
[48] S. Bhandari, R.A. Lopez-Anido, L. Wang, D.J. Gardner, Elasto-plastic finite element modeling of short carbon fiber reinforced 3D printed acrylonitrile butadiene styrene composites, Jom 72 (2020) 475–484, https://doi.org/10.1007/s11837-019-03895-w.
[49] E. Rusiński, D. Pietrusiak, A review of fused deposition modeling process models, Lect. Notes Mech. Eng. (2017) 241–246, https://doi.org/10.1007/978-3-319-50938-9.
[50] V. Basile, F. Modica, G. Fontana, S. Ruggeri, I. Fassi, Improvements in accuracy of fused deposition modeling via integration of low-cost on-board vision systems, J. Micro Nano-Manuf. 8 (2020) 1–6, https://doi.org/10.1115/1.4046038.
[51] D. Banabic, Sheet Metal Forming process: Constitutive modelling and Numerical Simulation (1. Aufl.), Springer-Verlag, 2010.
[52] Z. Mu, J. Zhao, Q. Meng, Y. Zhang, G. Yu, Limitation analysis of the Hill48 yield model and establishment of its modified model for planar plastic anisotropy, J. Mater. Process. Technol. 299 (2022) 117380, https://doi.org/10.1016/j.jmatprotec.2021.117380.
[53] U.W. Gedde and M.S. Hedenqvist, Fundamental polymer science, Second ed., 2019.
[54] Rubinstein, M.Colby, and R. H., Polymer physics. 2003. 10.3726/978-3-653-00025-2/5.
[55] A. Costanzo, et al., Residual alignment and its effect on weld strength in material-extrusion 3D-printing of polylactic acid, Addit. Manuf. 36 (2020) 101415, https://doi.org/10.1016/j.addma.2020.101415.
[56] W.M.H. Verbeeten, M. Lorenzo-Bañuelos, Material extrusion additive manufacturing of poly(Lactic Acid): influence of infill orientation angle, Addit. Manuf. 59 (2022) 103079, https://doi.org/10.1016/j.addma.2022.103079.
[57] C. McIlroy, P.D. Olmsted, Deformation of an amorphous polymer during the fused-filament-fabrication method for additive manufacturing, J. Rheol. (N. Y. N. Y). 61 (2017) 379–397, https://doi.org/10.1122/1.4976839.
[58] Q. Sun, G.M. Rizvi, C.T. Bellehumeur, P. Gu, Effect of processing conditions on the bonding quality of FDM polymer filaments, Rapid Prototyp. J. 14 (2008) 72–80, https://doi.org/10.1108/13552540810862028.
[59] R.P. Wool, K.M. O'Connor, A theory of crack healing in polymers, J. Appl. Phys. 52 (1981) 5953–5963, https://doi.org/10.1063/1.328526.
[60] Y.S. Ko, D. Herrmann, O. Tolar, W.J. Elspass, C. Brändli, Improving the filament weld-strength of fused filament fabrication products through improved interdiffusion, Addit. Manuf. 29 (2019) 100815, https://doi.org/10.1016/j.addma.2019.100815.
[61] J.E. Seppala, K.D. Migler, Infrared thermography of welding zones produced by polymer extrusion additive manufacturing, Addit. Manuf. 12 (2016) 71–76, https://doi.org/10.1016/j.addma.2016.06.007.
[62] M.M. Garmabi, P. Shahi, J. Tjong, M. Sain, 3D printing of polyphenylene sulfide for functional lightweight automotive component manufacturing through enhancing interlayer bonding, Addit. Manuf. 56 (2022) 102780, https://doi.org/10.1016/j.addma.2022.102780.